LETTER

doi:10.1038/nature13462

Strong contributions of local background climate to urban heat islands

Lei Zhao[1,2], Xuhui Lee[1,2], Ronald B. Smith[3] & Keith Oleson[4]

The urban heat island (UHI), a common phenomenon in which surface temperatures are higher in urban areas than in surrounding rural areas, represents one of the most significant human-induced changes to Earth's surface climate[1,2]. Even though they are localized hotspots in the landscape, UHIs have a profound impact on the lives of urban residents, who comprise more than half of the world's population[3]. A barrier to UHI mitigation is the lack of quantitative attribution of the various contributions to UHI intensity[4] (expressed as the temperature difference between urban and rural areas, ΔT). A common perception is that reduction in evaporative cooling in urban land is the dominant driver of ΔT (ref. 5). Here we use a climate model to show that, for cities across North America, geographic variations in daytime ΔT are largely explained by variations in the efficiency with which urban and rural areas convect heat to the lower atmosphere. If urban areas are aerodynamically smoother than surrounding rural areas, urban heat dissipation is relatively less efficient and urban warming occurs (and vice versa). This convection effect depends on the local background climate, increasing daytime ΔT by 3.0 ± 0.3 kelvin (mean and standard error) in humid climates but decreasing ΔT by 1.5 ± 0.2 kelvin in dry climates. In the humid eastern United States, there is evidence of higher ΔT in drier years. These relationships imply that UHIs will exacerbate heatwave stress on human health in wet climates where high temperature effects are already compounded by high air humidity[6,7] and in drier years when positive temperature anomalies may be reinforced by a precipitation–temperature feedback[8]. Our results support albedo management as a viable means of reducing ΔT on large scales[9,10].

The conversion of natural land to urban land causes several notable perturbations to the Earth's surface energy balance. Reduction of evaporative cooling is generally thought to be the dominant factor contributing to UHI. Anthropogenic heat release is an added energy input to the energy balance and should increase the surface temperature. Energy input by solar radiation will also increase if albedo is reduced in the process of land conversion. Buildings and other artificial materials can store more radiation energy in the daytime than can natural vegetation and soil; release of the stored energy at night contributes to night-time

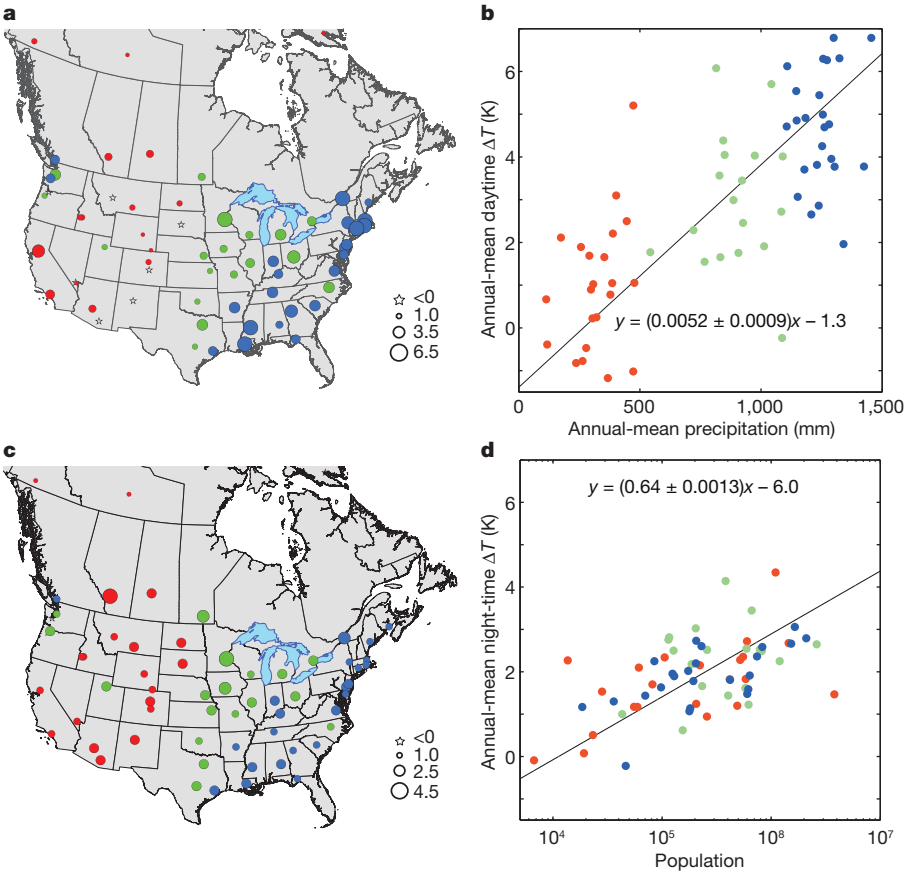

Figure 1 | Precipitation and population influences on MODIS-derived annual-mean UHI intensity. **a**, Map of daytime UHI (shown in K by symbol type/size). **b**, Dependence of daytime UHI on precipitation ($r = 0.74$, $P < 0.001$). **c**, Map of night-time UHI. **d**, Dependence of night-time UHI on population ($r = 0.54$, $P < 0.001$). Red, green and blue symbols denote cities with annual mean precipitations less than 500 mm, between 500 and 1,100 mm, and over 1,100 mm, respectively. Lines in **b** and **d** are linear regression fits to the data. Parameter bounds for the regression slope are the 95% confidence interval.

[1]Yale-NUIST Center on Atmospheric Environment, Nanjing University of Information Science and Technology, Nanjing 210044, China. [2]School of Forestry and Environmental Studies, Yale University, New Haven, Connecticut 06511, USA. [3]Department of Geology and Geophysics, Yale University, New Haven, Connecticut 06511, USA. [4]National Center for Atmospheric Research, Boulder, Colorado 80305, USA.

UHI. Finally, energy redistribution through convection between the surface and the atmospheric boundary layer can either increase or reduce ΔT, depending on whether the efficiency of convection over urban land is suppressed or enhanced relative to that over adjacent rural land. Although these concepts have been known for some time[11–13], a quantitative understanding of their roles across different climate regimes remains elusive[4].

The climatic context can be understood by posing the following question in a thought experiment: if two cities are built identically in terms of morphological and anthropogenic aspects but in different climates, will they have the same ΔT? The answer depends on time of day according to observations of surface temperature by the NASA MODIS satellite. For 65 selected cities in North America, the annual-mean midnight ΔT (surface temperature of urban core pixels minus that of rural pixels) is positively correlated with the logarithm of population (correlation coefficient, $r = 0.54$; confidence level, $P < 0.001$; Fig. 1d), but is invariant with climate, showing a statistically insignificant correlation with precipitation ($r = 0.05$, $P = 0.70$; Extended Data Fig. 1), solar radiation ($r = 0.15$, $P > 0.20$) and air temperature ($r = 0.20$, $P > 0.10$). However, the annual-mean midday ΔT is strongly correlated with precipitation ($r = 0.74$, $P < 0.001$; Fig. 1b) and has a weaker statistical dependence on population size than does the night-time ΔT ($r = 0.27$, $P = 0.027$; Extended Data Fig. 1). The night-time ΔT shows little spatial coherence (Fig. 1c), but the daytime ΔT has a discernible spatial pattern that follows precipitation gradients across the continent (Fig. 1a). Twenty-four of the cities are located in the humid southeast United States, which coincides roughly with the Köppen–Geiger temperate climate zone (Fig. 2a). Their daytime annual-mean ΔT is on average 3.9 K and is 3.3 K higher than that of the 15 cities in the dry region (Fig. 2d, e). By comparison, the night-time ΔT differs by 0.1 K between the two groups ($P > 0.60$; Fig. 2f, g). These results are in broad agreement with previous remote-sensing studies on UHI across biophysical and developmental gradients[14–17].

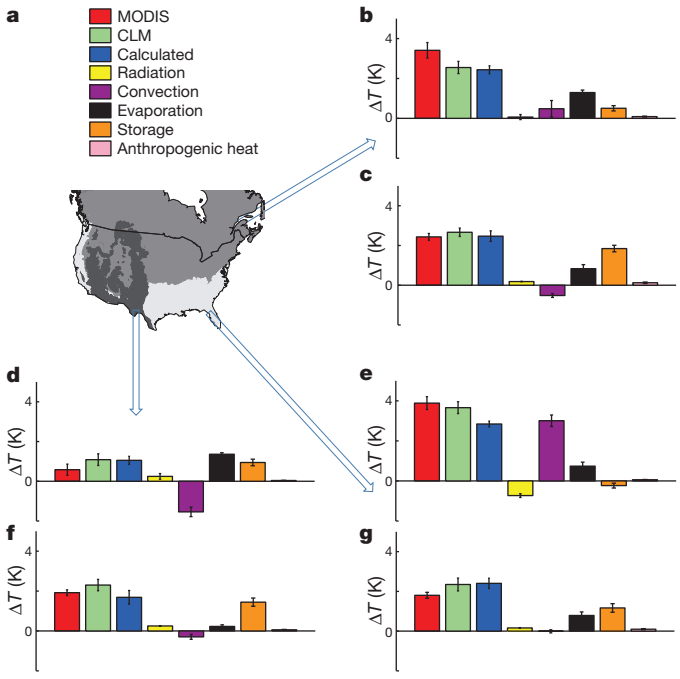

Figure 2 | Attribution of UHI intensity in three Köppen–Geiger climate zones. **a**, Map of climate zones: white, mild temperate/mesothermal climate; grey, continental /microthermal climate; dark grey, dry climate. **b**, **d**, **e**, Daytime values of MODIS and modelled ΔT and its component contributions in each of the three zones (see arrows). **c**, **f**, **g**, Night-time values in each of the three zones (see arrows). Green bars denote model-predicted ΔT and blue bars denote UHI intensity calculated as the sum of the component contributions. Error bars, 1 s.e. for each climate zone.

At first glance, the relationship with precipitation (Fig. 1b) seems consistent with the hypothesis that reduction in evaporative cooling in urban land is the main driver of daytime ΔT, because the denser vegetation in wet climate regions has a higher evaporation rate than the vegetation in dry climates. However, our model-based analysis does not support such an interpretation. In the model domain, ΔT is a perturbation signal to the surface temperature caused by biophysical contrast between rural and urban land units in the same model grid cell[18]. This signal is further decomposed, using the method described in ref. 19, into contributions from changes in radiation balance, evaporation, convection efficiency and heat storage, and from anthropogenic heat addition (Fig. 2). The credibility of the model is supported by the reasonable agreement of the modelled ΔT with the MODIS ΔT ($r = 0.31$, $P < 0.02$ for daytime; $r = 0.30$, $P < 0.025$ for night time) and by its accurate depiction of the relationship between night-time ΔT and albedo (Extended Data Fig. 4). Furthermore, the model has reproduced the observed positive correlation between the daytime ΔT and precipitation (Fig. 3a).

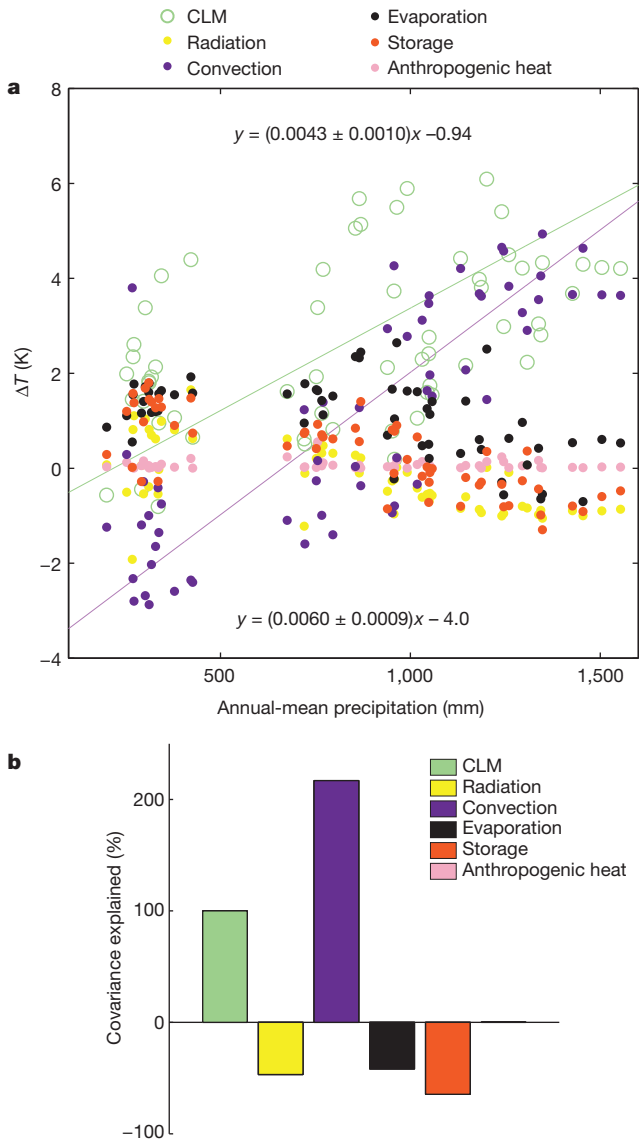

Figure 3 | Relationship between model-predicted daytime ΔT and precipitation among the cities. **a**, Correlation of ΔT and the individual biophysical components with annual-mean precipitation. Lines are linear regression fits to the corresponding data. Parameter bounds for the regression slope are the 95% confidence interval. **b**, ΔT–precipitation covariance explained by different biophysical factors. Note that the covariance explained by the anthropogenic heat term is negligibly small.

We find that it is the changes in convection efficiency (associated with aerodynamic resistance changes), rather than those in evapotranspiration, that control the daytime ΔT–precipitation spatial covariance among the cities (Fig. 3). In the humid climate (the Köppen–Geiger temperate climate zone), convection is less efficient at dissipating heat from urban land than from rural land, and the associated temperature increase is 3.0 ± 0.3 K, which dominates the overall ΔT (Fig. 2e). At these locations, the rural land is in general densely vegetated, owing to ample precipitation, and is aerodynamically rough. Quantitatively, this difference is manifested in a lower aerodynamic resistance to sensible heat diffusion in the rural land ($39\ s\ m^{-1}$) than in the urban land ($62\ s\ m^{-1}$). Measured in terms of aerodynamic resistance, urbanization has reduced the convection efficiency by 58%.

The opposite occurs in the dry climate zone, where urban land is rougher than rural land and has enhanced convection efficiency. The result is actually a cooling effect (Fig. 2d). In this zone, the urban landscape has lower aerodynamic resistance ($53\ s\ m^{-1}$) than the adjacent rural land ($66\ s\ m^{-1}$), which is typically inhabited by vegetation of low stature such as shrubs, sagebrushes and grasses. On average, the urban land is about 20% more efficient in removing heat from the surface by convection than is the rural land. The average cooling signal is -1.5 ± 0.2 K. In a few of the cities, convection is much more efficient than in the surrounding natural land, such that ΔT becomes negative (Figs 1a and 3a). It has been suggested that negative ΔT, a phenomenon known as 'urban heat sink', arises from evaporative cooling of trees and lawns planted in the city[15–17]. Our explanation seems more logical, because the MODIS urban temperature comes from the urban core pixels with negligible amounts of vegetation cover (enhanced vegetation index, <0.18) and the urban land unit in the climate model is completely free of vegetation. An analogous situation exists in a semi-arid plantation forest where trees serve as efficient 'heat convectors', leading to a lower surface temperature than in the adjacent smoother shrub land[20].

At night, release of the stored heat is the dominant contributor to ΔT across all three climate zones (Fig. 2c, f and g). The dependence on population size (Fig. 1d), which is an indicator of the city's horizontal dimension, can be understood in light of these results. At night, the released heat is trapped in a very shallow atmospheric boundary layer. As air moves across the urban land, it will accumulate more heat with increasing travel distance. Having a longer upwind fetch, that is, a longer distance between the upwind edge of the city and the point of observation, the centre of a larger city should experience stronger warming[11].

There is some evidence of precipitation control on interannual variability in the daytime ΔT for individual cities. For each city, we have calculated the linear regression slope of the annual daytime ΔT against the annual precipitation, and we refer to it as the temporal sensitivity to precipitation. Both the MODIS and the model data show a negative dependence of the sensitivity on site mean precipitation (Fig. 4b, d). Twenty-four cities have annual-mean precipitation exceeding 1,100 mm. According to the model, all of these cities, which are mostly distributed in the eastern United States, have negative temporal sensitivity (Fig. 4c), meaning higher ΔT in drier years. The mean temporal sensitivity of this group of cities is $-0.0021\ K\ mm^{-1}$. The MODIS results are less consistent because of shorter data records, showing negative sensitivity for 42% of them (Fig. 4a, b).

To gain further insight into the interannual variability, we have compared the daytime ΔT–precipitation correlations for Billings in Montana (annual-mean precipitation, 353 mm) and Richmond in Virginia (1,183 mm). We choose these two cities because they have nearly the same morphological and biophysical specifications (Extended Data Table 1) and therefore are essentially identical in the model world. The sensitivity to precipitation is positive at Billings and negative at Richmond (Extended Data Fig. 2). In contrast to the spatial variations across North America (Fig. 3b), the ΔT interannual variability shown here is driven primarily by changes in surface evaporation (Extended Data Fig. 3).

Our results can be interpreted in the context of heatwave climatology. A measure of heatwave intensity is the degree of deviation, in multiples of standard deviation (North American mean value, $\sigma \approx 0.6$ K) of summertime temperature from the climatological mean[21]. For example, the 2003 European heatwave[8] is a rare event measured at 5σ. These statistical considerations are based on regional background climatology. Being an additional anomaly on this background condition, UHI will aggravate heat stress on human health. In the southeast United States, where the heat stress is already amplified by high air humidity[7], the daytime ΔT is equivalent to 7σ (Fig. 2e). The situation may be further

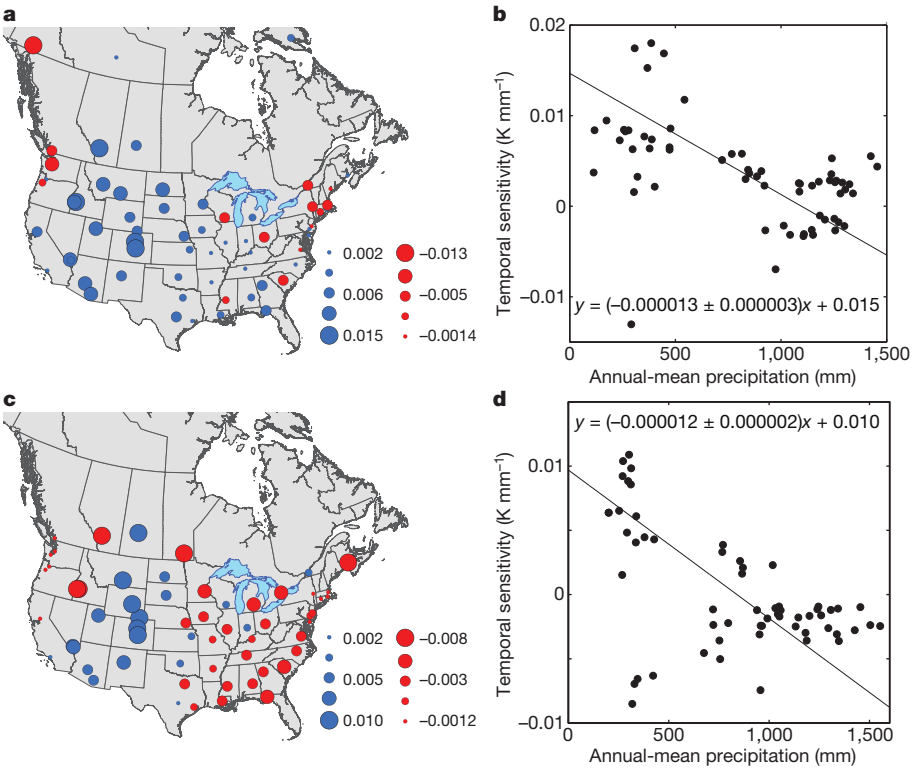

Figure 4 | Temporal sensitivity of UHI intensity to precipitation. **a**, **c**, Map of the temporal sensitivities (shown in $K\ mm^{-1}$ by symbol size) according to MODIS (**a**) and the climate model (**c**). **b**, **d**, Dependence of MODIS (**b**) and model-predicted (**d**) temporal sensitivity on annual mean precipitation. The outlier city in the MODIS panels is Whitehorse in Yukon. The four outlier cities in the model panels are Boise and Nampa in Idaho, Winnipeg in Manitoba and Calgary in Alberta. Lines in **b** and **d** are linear regression fits to the data. Parameter bounds for the regression slope are the 95% confidence interval.

worsened in drier years when the positive temperature anomaly is likely to increase owing to a precipitation–temperature feedback[8]. Empirical evidence exists for such synergistic effects[22]. Using the temporal sensitivity of $-0.0021\ \mathrm{K\ mm^{-1}}$, a 500 mm reduction in the annual precipitation corresponds to an increase in the daytime ΔT by 1.1 K, or $\sim 2\sigma$. We caution that these numbers represent the upper bound of the UHI-added stress because UHI intensity at the screen height[23] (the height of air temperature observation at a standard weather station) and under all-sky conditions should be smaller than our ΔT, which is for clear skies and for the surface. However, summertime ΔT is generally larger than annual ΔT (refs 13–17, 24).

The health impact of heatwaves is one factor that motivates the growing efforts to mitigate UHI. According to our results, a strategy that focuses on reducing anthropogenic heat would bring virtually no relief, but this might be because of the primitive anthropogenic heat scheme in the model[18]. Managing the convection efficiency or heat storage of urban land does not seem viable, even though these are large contributors to ΔT, because it would require fundamental changes to the urban morphology, such as a city-wide increase in building height. However, efforts to increase urban albedo have the promise of producing measurable results on a large scale. For the cities in the southern United States, the reduction of net radiation loading amounts to a daytime cooling effect of 0.7 K (Fig. 2e). In the model, this reduction is caused by the fact that these cities have an average albedo that is 0.06 higher than the surrounding rural land. This albedo difference is modest, considering that phasing in reflective roofs in Chicago[25] has already increased the city-wide albedo by $\sim$0.02 and that some cool-roof implementations[10] aim to increase the urban–rural albedo contrast by as much as 0.6. Albedo increases have little direct effect on the night-time UHI (Fig. 2g) but may have an indirect cooling benefit through the reduction in the daytime heat storage and, therefore, less heat release from storage at night[16,26,27]. The negative correlation between the night-time ΔT and urban–rural albedo contrast[16] (Extended Data Fig. 4) can be viewed as empirical evidence of this indirect benefit.

METHODS SUMMARY

MODIS data. We calculated the annual-mean ΔT using the MODIS-Aqua eight-day composite land surface temperature from 2003 to 2012. The night-time and daytime ΔT were determined at 1:30 and 13:30 local time, respectively. Data were collected at 65 cities distributed across the United States and Canada. For each city, we paired pixels in the centre of the city with those outside the city to determine ΔT.
Climate model. We used the Community Earth System Model[28] to simulate UHI. The model grid cell consists of urban and rural land units whose surface energy balance variables are calculated using a single-layer urban surface parameterization and a standard land surface scheme, respectively[18,29]. We ran the model for 33 yr of simulation time from 1972 to 2004 after a 60 yr spin-up. The forcing data are an atmospheric reanalysis product validated against various observations[30]. The simulation was conducted at the finest resolution supported by the model (0.23° longitude $\times$ 0.31° latitude) to resolve individual cities. The surface skin temperature was determined from the emitted long-wave radiation. To be consistent with the MODIS observations, we used the modelled data at 1:00 and 13:00 local time and under clear-sky conditions to compute the annual ΔT and to perform the surface energy balance analysis.
Attribution of UHI. Attribution of UHI is accomplished by a surface energy balance analysis. The total ΔT is partitioned, using the method of ref. 19, into contributions from the differences, between the urban and rural land units, in surface radiation balance, convection efficiency, evapotranspiration and heat storage, and from anthropogenic heat addition. The perturbation to the radiation balance results mainly from albedo contrast and also includes a minor part associated with surface emissivity change. The analysis was done separately for daytime and night time using the relevant forcing and prognostic model variables.

Online Content Methods, along with any additional Extended Data display items and Source Data, are available in the online version of the paper; references unique to these sections appear only in the online paper.

Received 19 January; accepted 7 May 2014.

1. Kalnay, E. & Cai, M. Impact of urbanization and land-use change on climate. *Nature* **423,** 528–531 (2003).
2. Zhou, L. M. *et al.* Evidence for a significant urbanization effect on climate in China. *Proc. Natl Acad. Sci. USA* **101,** 9540–9544 (2004).
3. Grimm, N. B. *et al.* Global change and the ecology of cities. *Science* **319,** 756–760 (2008).
4. Voogt, J. A. & Oke, T. R. Thermal remote sensing of urban climates. *Remote Sens. Environ.* **86,** 370–384 (2003).
5. Taha, H. Urban climates and heat islands: albedo, evapotranspiration, and anthropogenic heat. *Energy Build.* **25,** 99–103 (1997).
6. Fischer, E. M. & Schär, C. Consistent geographical patterns of changes in high-impact European heatwaves. *Nature Geosci.* **3,** 398–403 (2010).
7. Smith, T. T., Zaitchik, B. F. & Gohlke, J. M. Heat waves in the United States: definitions, patterns and trends. *Clim. Change* **118,** 811–825 (2013).
8. Schär, C. *et al.* The role of increasing temperature variability in European summer heatwaves. *Nature* **427,** 332–336 (2004).
9. Akbari, H., Menon, S. & Rosenfeld, A. Global cooling: increasing world-wide urban albedos to offset CO_2. *Clim. Change* **94,** 275–286 (2009).
10. Georgescu, M., Moustaoui, M., Mahalov, A. & Dudhia, J. Summer-time climate impacts of projected megapolitan expansion in Arizona. *Nature Clim. Change* **3,** 37–41 (2013).
11. Oke, T. R. The energetic basis of the urban heat-island. *Q. J. R. Meteorol. Soc.* **108,** 1–24 (1982).
12. Grimmond, S. Urbanization and global environmental change: local effects of urban warming. *Geogr. J.* **173,** 83–88 (2007).
13. Arnfield, A. J. Two decades of urban climate research: a review of turbulence, exchanges of energy and water, and the urban heat island. *Int. J. Climatol.* **23,** 1–26 (2003).
14. Roth, M., Oke, T. R. & Emery, W. J. Satellite-derived urban heat islands from 3 coastal cities and the utilization of such data in urban climatology. *Int. J. Remote Sens.* **10,** 1699–1720 (1989).
15. Imhoff, M. L., Zhang, P., Wolfe, R. E. & Bounoua, L. Remote sensing of the urban heat island effect across biomes in the continental USA. *Remote Sens. Environ.* **114,** 504–513 (2010).
16. Peng, S. S. *et al.* Surface urban heat island across 419 global big cities. *Environ. Sci. Technol.* **46,** 696–703 (2012).
17. Clinton, N. & Gong, P. MODIS detected surface urban heat islands and sinks: global locations and controls. *Remote Sens. Environ.* **134,** 294–304 (2013).
18. Oleson, K. Contrasts between urban and rural climate in CCSM4 CMIP5 climate change scenarios. *J. Clim.* **25,** 1390–1412 (2012).
19. Lee, X. *et al.* Observed increase in local cooling effect of deforestation at higher latitudes. *Nature* **479,** 384–387 (2011).
20. Rotenberg, E. & Yakir, D. Contribution of semi-arid forests to the climate system. *Science* **327,** 451–454 (2010).
21. Hansen, J., Sato, M. & Ruedy, R. Perception of climate change. *Proc. Natl Acad. Sci. USA* **109,** E2415–E2423 (2012).
22. Li, D. & Bou-Zeid, E. Synergistic interactions between urban heat islands and heat waves: the impact in cities is larger than the sum of its parts. *J. Appl. Meteorol. Climatol.* **52,** 2051–2064 (2013).
23. Gallo, K. P., Adegoke, J. O., Owen, T. W. & Elvidge, C. D. Satellite-based detection of global urban heat-island temperature influence. *J Geophys Res.* **107,** 4776 (2002).
24. Tran, H., Uchihama, D., Ochi, S. & Yasuoka, Y. Assessment with satellite data of the urban heat island effects in Asian mega cities. *Int. J. Appl. Earth Obs. Geoinf.* **8,** 34–48 (2006).
25. Mackey, C. W., Lee, X. & Smith, R. B. Remotely sensing the cooling effects of city scale efforts to reduce urban heat island. *Build. Environ.* **49,** 348–358 (2012).
26. Oleson, K. W., Bonan, G. B., Feddema, J. & Vertenstein, M. An urban parameterization for a global climate model. Part II: sensitivity to input parameters and the simulated urban heat island in offline simulations. *J. Appl. Meteorol. Climatol.* **47,** 1061–1076 (2008).
27. Rosenzweig, C. *et al.* Mitigating New York City's heat island: integrating stakeholder perspectives and scientific evaluation. *Bull. Am. Meteorol. Soc.* **90,** 1297–1312 (2009).
28. Hurrell, J. W. *et al.* The Community Earth System Model: a framework for collaborative research. *Bull. Am. Meteorol. Soc.* **94,** 1339–1360 (2013).
29. Oleson, K. *et al. Technical Description of Version 4.0 of the Community Land Model (CLM)* 257. Report No. NCAR/TN-478+STR (NCAR, 2010).
30. Qian, T. T., Dai, A., Trenberth, K. E. & Oleson, K. W. Simulation of global land surface conditions from 1948 to 2004. Part I: forcing data and evaluations. *J. Hydrometeorol.* **7,** 953–975 (2006).

Acknowledgements This research was supported by the Ministry of Education of China (grant PCSIRT), the Yale Climate and Energy Institute, the Yale Institute of Biospheric Studies, and a Yale University Graduate Fellowship. K.O. acknowledges support from NASA grant NNX10AK79G (the SIMMER project) and the NCAR WCIASP. NCAR is sponsored by the US National Science Foundation. The model simulations were supported by the Yale University Faculty of Arts and Sciences High Performance Computing Center.

Author Contributions X.L. designed the research. L.Z. carried out the model simulation and data analysis. R.B.S. contributed ideas to the research design. K.O. contributed ideas to the model simulation. X.L. and L.Z. drafted the manuscript.

Author Information Reprints and permissions information is available at www.nature.com/reprints. The authors declare no competing financial interests. Readers are welcome to comment on the online version of the paper. Correspondence and requests for materials should be addressed to X.L. (xuhui.lee@yale.edu).

METHODS

MODIS LST, precipitation and population data. The UHI temperature difference ΔT can be defined using shelter-derived air temperature or a satellite-derived radiative surface temperature. The former suffers from inhomogeneity in the urban landscape. The latter is a valuable spatial average, but is influenced by the emissivity of the surface. Neither exactly matches the human experience of UHI as an individual walks across the rural or urban landscape. For the purpose of comparing different cities, the surface temperature approach is easier and more stable. Nichol *et al.* (ref. 31) showed that the correlation between the surface and screen-height air temperature can be weak on neighbourhood scales and improves considerably at the scale of urban–rural transition.

MODIS Aqua land surface temperature (LST) data obtained at 65 cities in the United States and Canada were used in this analysis. This is an eight-day clear-sky composite data set. The spatial resolution is 1 km. The satellite overpass times are approximately 13:30 and 1:30 local time, which are close to the times of daily maximum and minimum temperature, and the measurement therefore gives a better representation of the diurnal range of ΔT than does that of the other MODIS satellite, Terra. According to the product quality control flag, the data we used have an average LST error less than or equal to 2 K. While selecting urban–rural paired pixels, we avoided the rural pixels that have large elevation differences and large latitude differences relative to the urban core. Specifically, the upper thresholds for elevation difference and latitude difference are 100 m and 0.1°. Nine urban pixels (3×3) were selected in the city centre, paired with 1–3 patches of 9–49 pixels each (3×3 to 7×7) in the surrounding rural land. Because of topographic and latitudinal limitations, the number of rural pixels varied (one patch for 15 cities, two patches for 41 cities and three patches for 9 cities). The magnitude of ΔT is insensitive to the number of urban–rural pixels. Fixing the number of urban and rural pixels for all the cities to one 3×3 patch of pixels altered ΔT by at most 0.6 K. All the pixels selected were validated by the MODIS land cover map and cross-checked against Google Earth. Rural pixels are classified in the MODIS land cover map as natural surfaces such as forests, grassland, cropland and bare soils. To avoid high bias of UHI, we excluded water pixels. Urban pixels are classified in the MODIS land cover map as urban and built-up surface. The resulting ΔT represents the difference between the city core and minimally developed land outside the city. The annual mean values were calculated based on the 10 yr time series of the MODIS LST (2003–2012). Linear gap filling was done for short periods of missing values to minimize the impact of missing data on the annual means. If there are more than three consecutive missing values, we excluded that year.

Cities were chosen so that each state, province or territory was represented by at least one city, with the exception of four provinces and a territory in Canada (Nova Scotia, Prince Edward Island and Newfoundland and Labrador; Extended Data Table 2). The chosen cities are large enough to be resolved by the climate model, except for five small cities (Helena, Montana; Augusta, Maine; Whitehorse, Yukon; Yellowknife, Northwest Territories; Iqaluit, Nunavut). These cities span a population range of 7,000–379,300. In addition, we avoided the cities on hilly terrain.

The US precipitation data were obtained from PRISM (PRISM Climate Group, Oregon State University; http://prism.oregonstate.edu). The precipitation data for cities in Canada were obtained from Environment Canada (http://climate.weather.gc.ca/). The PRISM data sets are elevation-corrected grid estimates of monthly, yearly and event-based climatic variables. The precipitation data for Canadian cities are station measurements.

The population data were obtained from the US Census 2010 (http://quickfacts.census.gov) and Canada 2011 Census from Statistics Canada (http://www12.statcan.gc.ca/census-recensement/2011/dp-pd/index-eng.cfm).

Climate model and simulation. We used NCAR's climate model CESM[28] (Community Earth System Model) to simulate the UHI in the United States and in Canada. In this model system, the land surface processes are represented by the Community Land Model[29] (CLM). We used CLM version 4.0. In CLM, the land surfaces are categorized into five land units: vegetation, glacier, wetland, urban and lake. Each grid cell can have one or more of these land units. The surface radiation and energy balance equations are solved separately for these land units, and the results are aggregated to yield grid cell means. Specifically, the urban land unit is modelled using a 'canyon' structure and consists of the following subsurfaces: roof, sunlit wall, shaded wall, and pervious (for example bare soil) and impervious (for example road, sidewalk and car park) canyon floor. It should be noted here that there is potentially more evaporation from the pervious canyon floor in the urban land unit than from the comparable bare soil in the rural land, because all of the water in the bare soil column is available for evaporation in the urban land unit. The vegetated land unit corresponds to nonurban or rural land. This land unit may contain up to 15 different plant functional types and bare soil.

The model was run in the offline mode (uncoupled from an active atmospheric model). The urban and rural parameterizations in each grid cell were driven by the same atmospheric forcing. The atmospheric forcing data used in this study is a careful reconstruction of the climatology from 1972 to 2004[30]. It was derived from a combination of the NCEP-NCAR reanalysis[32], observation-based analyses and observational records. Therefore, the data set has an improved accuracy compared with the NCEP-NCAR reanalysis. We ran the model for 33 yr from 1972 to 2004 after a 60 yr spin-up. The simulation was conducted at the finest resolution as a standard model configuration supported by this version of the model (0.23° longitude × 0.31° latitude), to resolve individual cities. We note that even at this finest resolution the grid cell is still large enough that the total urban area in a grid cell can be a combination of several urban areas. The surface skin temperature was determined from the emitted long-wave radiation for each land unit, with an emissivity of 0.88 for the urban land unit and 0.96 for the vegetated land unit. The urban emissivity is the mean value of the weighted averages of the emissivity values of the urban subsurfaces prescribed in the model for the selected cities. The rural emissivity is the mean value of the weighted average of the vegetation and soil emissivity.

To construct the UHI, urban and rural flux and state variables were extracted from the model output at the grid cells where the selected cities reside. CLM invokes the urban parameterization only if the urban area fraction exceeds a threshold of 0.1%. Therefore, five small cities used in the MODIS data analysis (Helena, Montana; Augusta, Maine; Whitehorse, Yukon; Yellowknife, Northwest Territories; Iqaluit, Nunavut) are neglected by the model.

We included only the modelled data at 1:00 and 13:00 local time each day in this analysis; these times were selected to match closely the MODIS overpass times. To replicate the MODIS clear-sky conditions, we excluded cloudy days whose clearness index[33] was less than 0.5. We then converted the daily values into eight-day averages. The gap filling and processes of calculating annual means are the same as for the MODIS data. Under all-sky conditions, the modelled UHI intensity is on average 0.59 K lower during the daytime and 0.02 K lower at night than the clear-sky values, and the pattern regarding the component contributions remains unchanged from the clear-sky plot (Fig. 2).

We note that the climate model cannot explicitly capture population dependence (Fig. 1). This is because population size is not a model parameter and the heat advection occurs at subgrid scales not resolved by its one-dimensional parameterization of land–atmosphere interactions.

Attribution of UHI. We used a surface energy balance analysis to isolate the contribution to the model-predicted ΔT from each individual biophysical factor associated with urban land conversion. In this analysis, the rural land is regarded as the base state, and urbanization is a perturbation to this base state. The perturbation signal is denoted by Δ. For example, $\Delta T = T_u - T_r$, where T_u is urban surface temperature and T_r is rural surface temperature within the same model grid cell. Following the method of ref. 19, the solution of the UHI intensity can be approximated by

$$\begin{aligned}\Delta T \approx & \frac{\lambda_0}{1+f}\Delta R_n^* + \frac{-\lambda_0}{(1+f)^2}(R_n^* - Q_s + Q_{AH})\Delta f_1 \\ & + \frac{-\lambda_0}{(1+f)^2}(R_n^* - Q_s + Q_{AH})\Delta f_2 + \frac{-\lambda_0}{1+f}\Delta Q_s \\ & + \frac{\lambda_0}{1+f}\Delta Q_{AH}\end{aligned} \quad (1)$$

with

$$f = \frac{\lambda_0 \rho C_p}{r_a}\left(1 + \frac{1}{\beta}\right)$$

$$R_n^* = (1-a)K_\downarrow + L_\downarrow - (1-\varepsilon)L_\downarrow - \varepsilon\sigma T_a^4$$

$$\Delta f_1 = \frac{-\lambda_0 \rho C_p}{r_a}\left(1 + \frac{1}{\beta}\right)\frac{\Delta r_a}{r_a}$$

$$\Delta f_2 = \frac{-\lambda_0 \rho C_p}{r_a}\frac{\Delta \beta}{\beta^2}$$

where T is the surface temperature, $\lambda_0 = 1/4\varepsilon\sigma T^3$ is the local climate sensitivity, f is the energy redistribution factor, R_n^* is the apparent net radiation, ρ is the air density, C_p is the specific heat of air at constant pressure, r_a is the aerodynamic resistance to heat diffusion, β is the Bowen ratio, a is the surface albedo, $K_\downarrow$ is the incoming solar radiation, $L_\downarrow$ is the incoming long-wave radiation, ε is the surface emissivity, σ is the Stefan–Boltzmann constant, T_a is the air temperature at a reference height. In this analysis, we assume that r_a, β, R_n* and Q_s and Q_{AH} are parameters associated with

the external perturbation (land use conversion) and are independent of T; the partial derivative of these variables can then be calculated.

In equation (1), the terms on the right-hand side represent, in order from the first to the last, contributions from changes in radiation balance (term 1), aerodynamic resistance (term 2), Bowen ratio (term 3), and heat storage (term 4) and from anthropogenic heat addition (term 5). Because r_a is the resistance to sensible or convection heat flux, term 2 is essentially a measure of change in the convection efficiency between urban and rural land. In an abstract sense, changes in β (term 3) can result from changes in sensible heat flux (H), latent heat flux (LE) or both (see equation (2), below). In the present context of partial differentiation, however, H and LE are not independent because the delta term Δf_2 is evaluated with the net radiation R_n^* and other valuables held constant. Thus, a reduction in β is accomplished by channelling more radiation energy to the surface latent heat flux, and it is appropriate to attribute term 3 to changes in surface evaporative cooling.

The calculation was performed separately for 1:00 and 13:00 local time, with cloudy days omitted. Three sets of variables were used. The first set comes directly from the forcing data and includes precipitation, incoming solar radiation ($K_\downarrow$), reference-height air temperature (T_a; air temperature at 30 m above the surface), air pressure and downward long-wave radiation ($L_\downarrow$). The second set has model-predicted variables, including reflected short-wave radiation ($aK_\downarrow$), sensible heat flux (H), latent heat flux (LE), storage heat flux (Q_s) and anthropogenic heat flux (Q_{AH}). The third set of variables, including surface temperature (T), air density (ρ), Bowen ratio (β) and aerodynamic resistance (r_a) were derived from the forcing data and the model-predicted variables. Specifically, the Bowen ratio was calculated as

$$\beta = \frac{H}{\mathrm{LE}} \tag{2}$$

and the aerodynamic resistance to heat diffusion was calculated from

$$r_a = \frac{\rho C_p (T - T_a)}{H} \tag{3}$$

The aerodynamic resistance determined from equation (3) is the sum of the diffusion resistance in the atmospheric surface layer and the excess resistance associated with the thermal roughness[34,35]. The urban and rural land units within each model grid cell have the same forcing variables and have different values for the second and third sets of the variables. It should be noted here that the model underestimates the anthropogenic heat flux (Q_{AH}) owing to the primitive anthropogenic heat scheme. The total anthropogenic heat in the model includes only heating and air conditioning (HAC) fluxes, waste heat generated by HAC and the heat removed by air conditioning. These fluxes are based on some prescribed parameters in the surface data set of CLM and calculated heat transfer into and out of roofs and walls. The heat flux due to traffic is neglected by the current version of the model[36].

The sum of the component contributions is slightly lower than the modelled ΔT (Fig. 2) because high-order terms are ignored in the linearization of the surface long-wave radiation term of the energy balance equation and nonlinear interactions among the factors are omitted in the analysis. Comparison between model-predicted ΔT and calculated ΔT (sum of the individual contributions) reveals excellent correlation for daytime ($r = 0.88$, $P < 0.001$) and night time ($r = 0.55$, $P < 0.001$).

Covariance analysis. The covariance analysis was performed on modelled ΔT and its components against precipitation. Let C_R, C_H, C_{LE}, C_s and C_{AH} be the contributions from radiation, convection efficiency, evaporation, storage and anthropogenic heat, respectively (terms 1 to 5 in equation (1)). Equation (1) can be rewritten as

$$\Delta T = C_R + C_H + C_{LE} + C_s + C_{AH} + e$$

where e is an error term arising from nonlinear interactions. Because the covariance operation is linear, the ΔT–precipitation covariance is equal to the sum of the covariance between each component and precipitation

$$\begin{aligned} \mathrm{Cov}(\Delta T, P) = {} & \mathrm{Cov}(C_R, P) + \mathrm{Cov}(C_H, P) \\ & + \mathrm{Cov}(C_{LE}, P) + \mathrm{Cov}(C_s, P) \\ & + \mathrm{Cov}(C_{AH}, P) + \mathrm{Cov}(e, P) \end{aligned} \tag{4}$$

where P is precipitation. Equation (4) decomposes the total covariance between ΔT and precipitation into the covariance contribution from its five components and a residual error term. We presented covariance here rather than correlation coefficient because the correlation is not a linear operation. In Fig. 3 and Extended Data Fig. 3, we normalized the covariance between each component and precipitation by the total ΔT–precipitation covariance.

We applied this technique to the analysis of both spatial covariance and temporal covariance. In the analysis of spatial covariance, each data point is the climatic annual mean value of a city (Fig. 3). In the analysis of the temporal covariance at a city, each data point is the mean value for an individual year of that city (Extended Data Fig. 3).

31. Nichol, J. *et al.* Urban heat island diagnosis using ASTER satellite images and 'in situ' air temperature. *Atmos. Res.* **94,** 276–284 (2009).
32. Kalnay, E. *et al.* The NCEP/NCAR 40-year reanalysis project. *Bull. Am. Meteorol. Soc.* **77,** 437–471 (1996).
33. Gu, L. H., Fuentes, J. D., Shugart, H. H., Staebler, R. M. & Black, T. A. Responses of net ecosystem exchanges of carbon dioxide to changes in cloudiness: results from two North American deciduous forests. *J. Geophys. Res., D, Atmospheres* **104,** 31421–31434 (1999).
34. Garratt, J. R. *The Atmospheric Boundary Layer* (Cambridge Univ. Press, 1994).
35. Voogt, J. A. & Grimmond, C. S. B. Modeling surface sensible heat flux using surface radiative temperatures in a simple urban area. *J. Appl. Meteorol.* **39,** 1679–1699 (2000).
36. Oleson, K. W., Bonan, G. B., Feddema, J. & Jackson, T. An examination of urban heat island characteristics in a global climate model. *Int. J. Climatol.* **31,** 1848–1865 (2011).

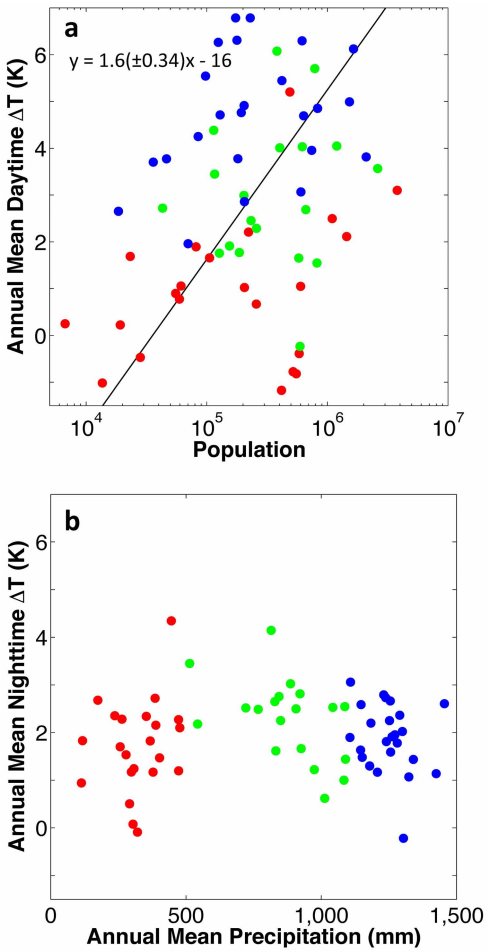

Extended Data Figure 1 | Precipitation and population influences on MODIS-derived annual mean UHI intensity. **a**, Dependence of daytime UHI on population size ($r = 0.27$, $P = 0.027$). **b**, Dependence of night-time UHI on precipitation ($r = 0.05$, $P = 0.70$). Red, green and blue symbols denote cities with annual mean precipitations less than 500 mm, between 500 and 1,100 mm, and over 1,100 mm, respectively. The solid line in **a** is the linear regression fit to the data. Parameter bounds for the regression slope are the 95% confidence interval.

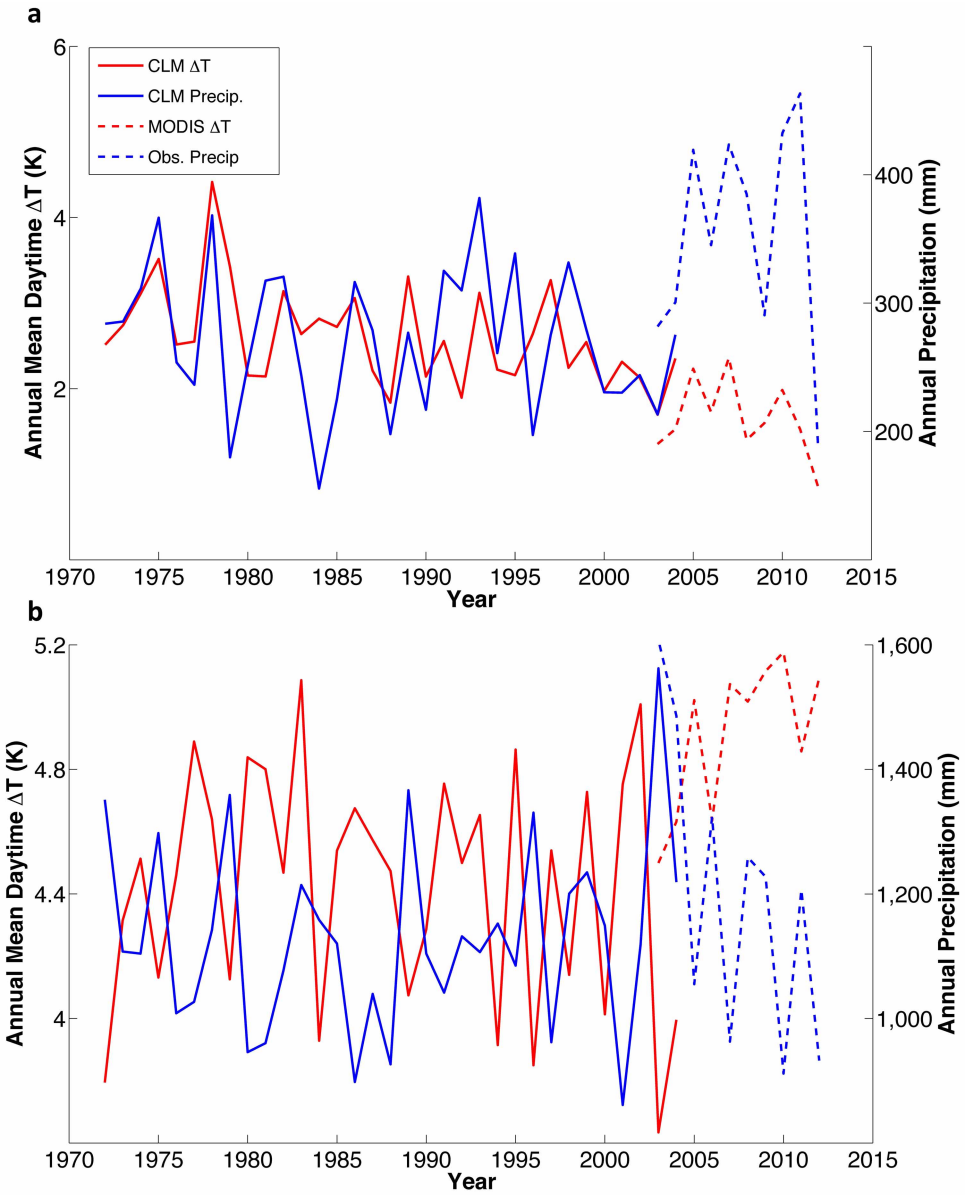

Extended Data Figure 2 | Time series of MODIS and model-predicted daytime Δ*T* and annual precipitation. **a**, Billings, Montana. **b**, Richmond, Virginia.

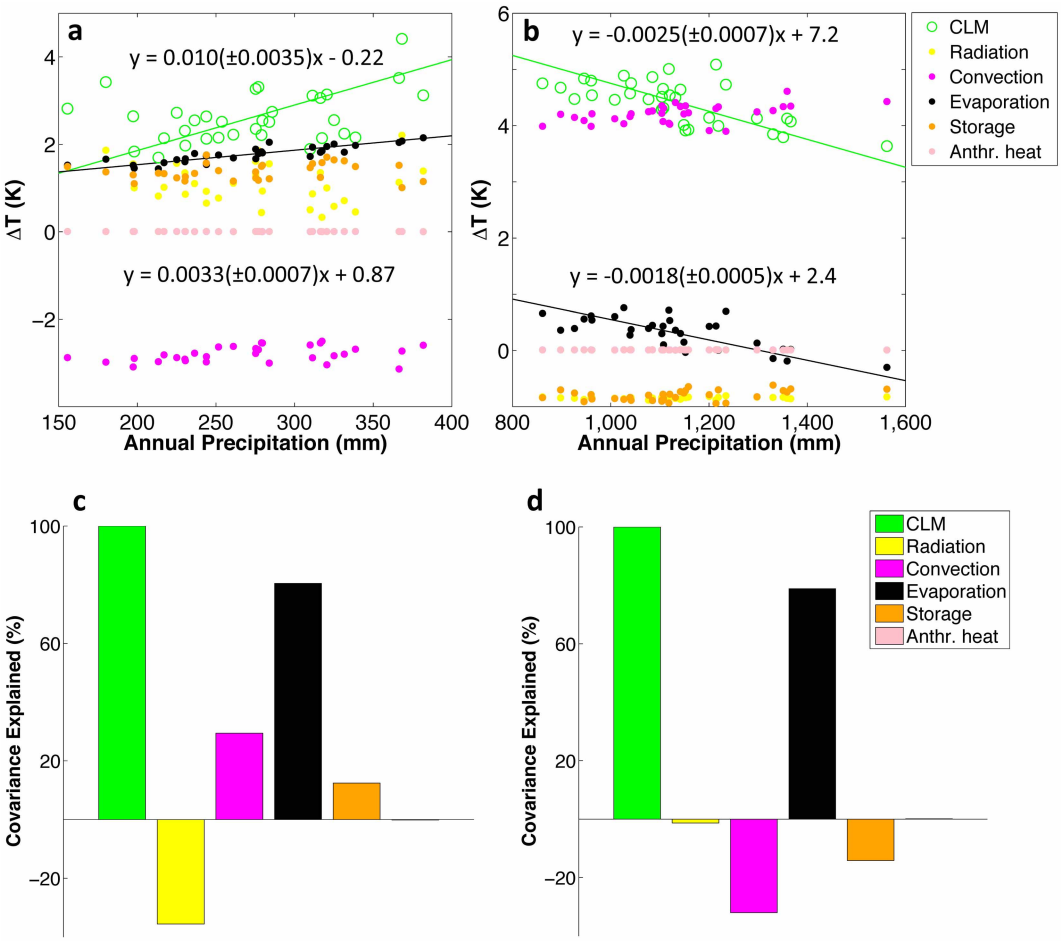

Extended Data Figure 3 | Relationship between interannual variations in model-predicted daytime ΔT and precipitation. **a**, Correlation of ΔT and the individual biophysical components with annual precipitation at Billings, Montana. **b**, Same as in **a** except for Richmond, Virginia. **c**, ΔT–precipitation temporal covariance explained by different biophysical factors at Billings, Montana. **d**, Same as in **c** except for Richmond, Virginia. Lines are best linear regression fits to the data points. Parameter bounds for the regression slope are the 95% confidence interval.

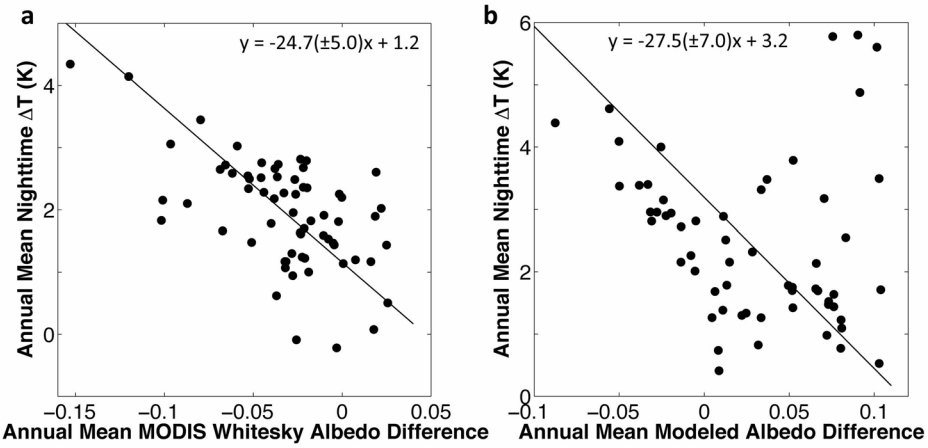

Extended Data Figure 4 | Albedo influence on annual mean night-time UHI intensity. **a**, Dependence of night-time MODIS-derived UHI on white-sky albedo difference (that is, urban albedo minus rural albedo; $r = -0.60$, $P < 0.001$). **b**, Dependence of night-time modelled UHI on modelled albedo difference ($r = -0.56$, $P < 0.001$ excluding four outliers; $r = -0.18$, $P = 0.16$ with all data points). The four outliers in the upper right corner of **b** are coastal cities (Olympia, Washington; Seattle, Washington; Salem, Oregon; Vancouver, British Columbia) that have high biases of the modelled ΔT compared to the MODIS ΔT. Lines are linear regression fits to the data. Parameter bounds for the regression slope are the 95% confidence interval.

Extended Data Table 1 | Urban parameters of a city pair in CLM

City	Richmond	Billings
State	Virginia	Montana
Latitude (^{o})	37.53	45.79
Longitude (^{o})	-77.42	-108.54
Canyon Height/Width	0.48	0.48
Mean building height (m)	12	12
Roof thickness (m)	0.15	0.15
Wall thickness (m)	0.28	0.28
Wind height in canyon (m)	6	6
Roof fraction	0.55	0.50
Pervious road fraction	0.66	0.64
Emissivity (Impervious road)	0.91	0.91
Emissivity (pervious road)	0.95	0.95
Emissivity (roof)	0.65	0.65
Emissivity (wall)	0.91	0.91
Albedo (Impervious road)	0.13	0.13
Albedo (pervious road)	0.08	0.08
Albedo (roof)	0.30	0.30
Albedo (wall)	0.34	0.34
Roof thermal conductivity (W m^{-1} K^{-1})	0.84	0.84
Wall thermal conductivity (W m^{-1} K^{-1})	1.06	1.06
Impervious road thermal conductivity (W m^{-1} K^{-1})	1.67	1.67
Layers of impervious road	2	2
Roof heat capacity (MJ m^{-3} K^{-1})	0.76	0.76
Wall heat capacity (MJ m^{-3} K^{-1})	0.81	0.81
Impervious road heat capacity (MJ m^{-3} K^{-1})	2.06	2.06

Extended Data Table 2 | Size statistics for selected cities in the United States and in Canada

City, State/Province	Population	City size in CLM (km^2)	City, State/Province	Population	City size in CLM (km^2)
Albany, NY	9.79E+04	15.45	Louisville, KY	7.41E+05	45.75
Albuquerque, NM	5.53E+05	25.24	Madison, WI	2.33E+05	22.73
Atlanta, GA	4.20E+05	117.03	Minneapolis, MN	3.83E+05	90.58
Augusta, ME	1.86E+04	NA	Montgomery, AL	2.06E+05	12.99
Austin, TX	8.21E+05	63.16	Montreal, QC	1.65E+06	41.10
Baton Rouge, LA	2.30E+05	17.70	Nampa, ID	8.16E+04	6.56
Billings, MT	1.06E+05	2.14	Nashville, TN	6.36E+05	30.35
Bismarck, ND	6.13E+04	6.05	Oklahoma City, OK	5.80E+05	10.72
Boise, ID	2.06E+05	12.84	Olympia, WA	4.65E+04	12.94
Boston, MA	6.18E+05	86.42	Philadelphia, PA	1.53E+06	71.51
Calgary, AB	1.10E+06	21.48	Phoenix, AZ	1.45E+06	53.91
Casper, WY	5.53E+04	3.33	Pierre, SD	1.36E+04	0.89
Cheyenne, WY	5.95E+04	2.46	Portland, OR	5.94E+05	54.50
Colorado Springs, CO	4.16E+05	29.43	Providence, RI	1.78E+05	16.06
Columbia, SC	1.29E+05	2.56	Raleigh, NC	4.04E+05	37.60
Columbus, OH	7.87E+05	14.55	Richmond, VA	2.04E+05	8.00
Dallas, TX	1.20E+06	153.98	Sacramento, CA	4.89E+05	36.27
Denver, CO	6.00E+05	75.02	Saint John, NB	7.01E+04	1.42
Des Moines, IA	2.03E+05	32.56	Salem, OR	1.55E+05	14.41
Dover, DE	3.60E+04	1.84	Salt Lake City, UT	1.86E+05	57.87
Hartford, CT	1.25E+05	25.03	Saskatoon, SK	2.22E+05	13.07
Helena, MT	2.82E+04	NA	Seattle, WA	6.21E+05	108.04
Henderson, NV	2.58E+05	31.46	Springfield, IL	1.16E+05	12.97
Houston, TX	2.10E+06	151.09	Tallahassee, FL	1.81E+05	7.58
Indianapolis, IN	8.30E+05	37.56	Topeka, KS	1.27E+05	5.16
Iqaluit, NU	6.70E+03	NA	Toronto, ON	2.62E+06	215.29
Jackson, MS	1.74E+05	15.76	Trenton, NJ	8.49E+04	36.53
Jefferson City, MO	4.31E+04	3.54	Tucson, AZ	5.20E+05	27.73
Lansing, MI	1.14E+05	6.47	Vancouver, BC	6.04E+05	129.04
Las Vegas, NV	5.84E+05	31.46	whitehorse, YT	2.33E+04	NA
Lincoln, NE	2.58E+05	17.24	Winnipeg, MB	6.64E+05	47.08
Little Rock, AR	1.94E+05	13.64	Yellowknife, NT	1.92E+04	NA
Los Angeles, CA	3.79E+06	213.56			